Editors' Suggestion

Resonant x-ray diffraction study using circularly polarized x rays on antiferromagnetic TbB_4

R. Misawa,[1] K. Arakawa,[1] T. Yoshioka,[1] H. Ueda,[2] F. Iga,[3] K. Tamasaku,[4] Y. Tanaka,[4] and T. Kimura[1,5]

[1]*Department of Advanced Materials Science, University of Tokyo, Kashiwa, Chiba 277-8561, Japan*
[2]*SwissFEL, Paul Scherrer Institute, Forschungsstrasse 111, 5232 Villigen, Switzerland*
[3]*Graduate School of Science and Engineering, Ibaraki University, Mito 310-8512, Japan*
[4]*RIKEN SPring-8 Center, Sayo, Hyogo 679-5148, Japan*
[5]*Department of Applied Physics, University of Tokyo, Tokyo 113-8656, Japan*

(Received 21 August 2023; accepted 4 October 2023; published 24 October 2023)

Resonant x-ray diffraction (RXD) measurements at the Tb L_3 and the M_5 edges were carried out on a single crystal of a rare-earth tetraboride, TbB_4, which exhibits antiferromagnetic (AFM) order breaking both space-inversion and time-reversal symmetries. Considering its crystallographic and magnetic symmetries, both the anisotropic tensor of susceptibility (ATS) scattering and the magnetic scattering contribute to space-group-forbidden *odd*00 reflections under the resonant conditions in the AFM phase. We found that the RXD intensity of *odd*00 reflections depends on the helicity of the circularly polarized incident x rays, which is reasonably explained in terms of the interference effect between the ATS and the magnetic scatterings. Furthermore, the circular dichroic RXD showed a sample-position dependence, which reflects spatial distributions of AFM domains in TbB_4. Our study reveals that RXD using circularly polarized x rays is a powerful technique to probe not only the magnitude but also the sign of AFM order parameters and to spatially resolve AFM domains in materials breaking both space-inversion and time-reversal symmetries.

DOI: 10.1103/PhysRevB.108.134433

I. INTRODUCTION

Rare-earth borides have attracted continuous interest in the fields of both condensed matter physics and practical applications because of their refractory character and their largely specific structural and physical properties [1–3]. They show a variety of unusual electronic and magnetic properties such as superconductivity, frustrated magnetism, and electric quadrupolar order. Rare-earth tetraborides RB_4 (R = rare-earth elements), a class of rare-earth borides, crystalize in a tetragonal structure and have been extensively studied from a viewpoint of the geometrical frustration of magnetic dipoles [4–7] and electric quadrupole order of $4f$ electrons [8–11]. Furthermore, the rare-earth tetraborides are also discussed as systems allowing a linear magnetoelectric (ME) effect because magnetic structures in some of them break both time-reversal and space-inversion symmetries [12–14]. By the group-theoretical classification theory of multipole order, some of the rare-earth tetraborides are listed as odd-parity magnetic multipole materials allowing the ME effect and the magnetopiezoelectric effect [15].

TbB_4 is one of the rare-earth tetraborides and exhibits two successive magnetic phase transitions [16]. At $T_{N1} = 44$ K, TbB_4 shows a noncollinear antiferromagnetic (AFM) order in which Tb moments are aligned along the ⟨110⟩ directions with the propagation vector of $\mathbf{Q} = \mathbf{0}$, as depicted in Fig. 1(a) (AFM1 phase). The magnetic point group of the AFM1 phase is $4/m'm'm'$, which breaks both time-reversal and space-inversion symmetries and leads to a pair of AFM domains that transform into each other by either time-reversal or space-inversion operations [Fig. 1(a)]. Below $T_{N2} = 24$ K, the Tb moments are slightly tilted toward the a or b axis, as depicted in Fig. 1(b) (AFM2 phase). As a result, the fourfold symmetry is broken and the magnetic point group transforms into $m'm'm'$, which also breaks both time-reversal and space-inversion symmetries [16]. The transition at T_{N2} is considered to originate from a ferro-type order of electric quadrupole moments of Tb $4f$ electrons [17] and leads to additional orientational-type AFM domains as illustrated in Fig. 1(b).

In this study, we examine the AFM transitions and the AFM order parameters in TbB_4 by resonant x-ray diffraction (RXD) at the Tb L_3 and the M_5 edges using circularly polarized x rays. In TbB_4, the twofold screw axis along the [100] direction makes *odd*00 reflections forbidden. Under resonant conditions, however, the electric susceptibility of an absorbent atom at the $E1$-$E1$ transition is anisotropic, and a diffraction phenomenon called anisotropic tensor susceptibility (ATS) scattering [18] is active at the forbidden *odd*00 reflections. In both the AFM1 and the AFM2 phases, magnetic scattering is superimposed on the ATS scattering at *odd*00 reflections under the resonant conditions, which was reported in a previous RXD study in the vicinity of the Tb M_5 edge [19]. It has been reported that the interference effect between the magnetic scattering and the charge (or ATS) scattering leads to circular dichroism of RXD and allows the observation of time-reversal domains in some AFM materials [20,21]. We adopt this technique to detect AFM order parameters and distinguish AFM domains in the noncollinear antiferromagnet TbB_4 breaking both the time-reversal and space-inversion symmetries.

II. EXPERIMENT

A single crystal of TbB_4 was grown by the floating zone method using a mirror furnace equipped with four xenon

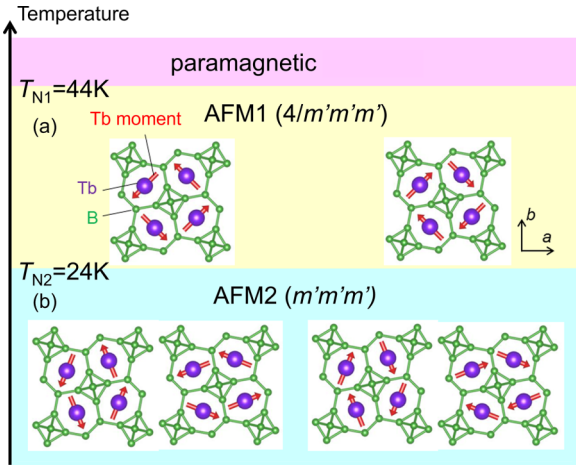

FIG. 1. Magnetic structures of TbB_4. (a) In the AFM1 phase ($T_{N2} < T < T_{N1}$), Tb moments are aligned along the ⟨110⟩ directions, and fourfold symmetry is preserved. There are two domain states which are converted into each other by either the time-reversal operation or the space-inversion operation. (b) In the AFM2 phase ($T < T_{N2}$), the fourfold symmetry is broken, and four domain states are present. Magnetic point groups of the respective phases are also shown.

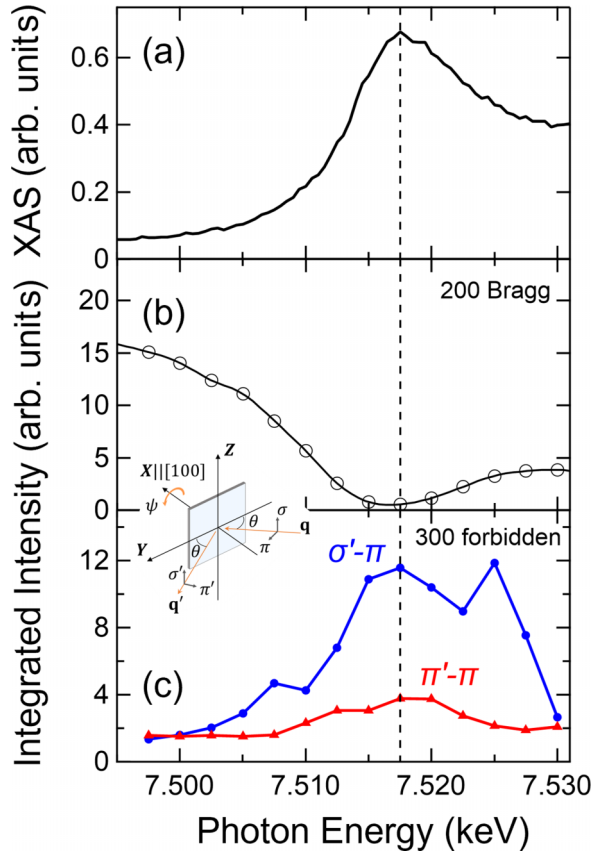

FIG. 2. Photon energy profiles in the vicinity of the Tb L_3 edge in TbB_4. (a) X-ray absorption spectrum (XAS). (b) Integrated intensity of the 200 Bragg reflection. (c) Integrated intensity of the 300 forbidden reflection for the $\sigma'-\pi$ and the $\pi'-\pi$ channels at $\psi = -90^\circ$. These data were taken at temperatures below T_{N1}. The dashed line indicates the photon energy ($E_{ph} = 7.5175$ keV) used for the experiments of Figs. 3 and 4. Inset: The scattering geometry of our resonant x-ray diffraction measurements. Here θ denotes the Bragg angle. The origin of azimuthal angle ($\psi = 0$) is defined as the condition that the c axis is perpendicular to the scattering plane.

lamps [22,23]. The orientation of the crystal was determined by Laue x-ray diffraction measurements. The crystal was cut into a thin plate ($\sim 2 \times 3 \times 0.5\,\mathrm{mm}^3$) with the widest faces parallel to the (100) plane. One of the surfaces was mechanically polished by using diamond slurries with an average particle size of 0.25 μm. Magnetization measurements confirmed that the crystal exhibits two magnetic transitions at $T_{N1} = 44$ K and $T_{N2} = 24$ K, which is consistent with previous reports [16,17].

RXD experiments using photon energies near the Tb L_3 and M_5 absorption edges were performed at beamlines 19LXU and 17SU, respectively, in SPring-8, Japan. A schematic drawing of the diffraction setup is shown in the inset of Fig. 2. Here θ denotes the Bragg angle. The [100] direction of the TbB_4 crystal was set along the momentum transfer vector ($\boldsymbol{\tau} = \mathbf{q} - \mathbf{q}'$) where $\mathbf{q}$ and $\mathbf{q}'$ are the wave vectors of the incident and the diffracted x rays, respectively. The rotation of the sample about $\boldsymbol{\tau}$ is defined as the azimuthal angle ψ. The origin of ψ was set at the condition of [001] perpendicular to the scattering plane.

For the experiments using hard x rays near the Tb L_3 edge, the circular polarization of incident x rays was manipulated by a diamond phase retarder [24]. We employed the 220 reflection of the diamond crystal with its surface being parallel to (001) and slightly detuned from the diffraction condition to obtain circular polarization. In the measurements for linearly polarized incident x rays, polarization analysis of diffracted x rays was carried out by using a graphite (006) analyzer crystal, which gave a scattering angle of 95.1° for the incident photon energy set at the Tb L_3 edge. By rotating the graphite crystal around the scattered beam, the linearly polarized σ (perpendicular to the scattering plane) and π (parallel to the scattering plane) components were separated. A silicon drift detector (XR-100SDD, Amptek Inc.) was utilized to suppress background signals due to x-ray photoemission and multiple scattering by higher harmonics from the beam source. The beam size of incident x rays was set at $0.2 \times 0.2\,\mathrm{mm}^2$ by upstream slits. The analyzer window was shaped by downstream slits in front of the graphite analyzer and was set at $0.2 \times 0.2\,\mathrm{mm}^2$. For measurements of sample-position dependence, a pinhole collimator (hole size $\sim 20 \times 20\,\mu\mathrm{m}^2$) was placed in front of the sample and the sample was positioned with an *XYZ* translation stage. To determine the resonance energy, x-ray absorption spectrum (XAS) around the Tb L_3 edge was obtained by measuring x-ray fluorescence.

For the experiments using soft x rays in the vicinity of the Tb M_5 edge, an upgraded diffractometer based on the prototype instrument [25] was utilized. Both unfocused and focused x-ray beams were used for the soft x-ray experiments. The unfocused x-ray beam was with an irradiation area of approximately 1 mm in horizontal and 0.8 mm in vertical directions. For scanning microdiffraction measurements, the incident beam was focused horizontally to a size of 25 μm and vertically to 10 μm by the upstream Kirkpatrick-Baez mirrors.

A silicon photodiode was used to detect diffracted x rays. The polarization of incident x rays was switched by a combination of electromagnets and permanent magnets, employing a multipolarization-mode undulator [26]. The degree of the circular polarization of the incident x rays was $|P_2| \geqslant 0.90$ in which P_2 is the Poincaré-Stokes parameter. The polarization state with $P_2 = +1$ corresponds to right-handed circularly polarized (RCP) x rays while that with $P_2 = -1$ means left-handed circularly polarized (LCP) ones. To measure spatial distributions of the diffracted intensity, the sample was positioned with an *XYZ* translation stage, as for the hard x-ray experiments. The azimuthal angle was fixed at $\psi = -90^\circ$ for the experiments in the vicinity of the Tb M_5 edge. XAS around the Tb M_5 edge was obtained by measuring x-ray fluorescence yield using a silicon drift detector.

III. FORMULATION OF RESONANT X-RAY DIFFRACTION

A. Formulation of the ATS scattering factor

First, the crystal structure factor of TbB_4 is calculated. In TbB_4 (space group: *P*4/*mbm*), Tb atoms are at the Wycoff position of 4*g* with the site symmetry *m*.2*m*. The positions of four Tb atoms in a unit cell are $(x, x+1/2, 0)$ for Tb(1), $(x+1/2, -x, 0)$ for Tb(2), $(-x, -x+1/2, 0)$ for Tb(3), and $(-x+1/2, x, 0)$ for Tb(4) where $x = 0.3172$ [16]. For $\boldsymbol{\tau} = (2n+1, 0, 0)$ where n is an integer, the Fourier component $\sum_j e^{2\pi i \boldsymbol{\tau}\cdot\mathbf{R}_j}$ is zero [$\mathbf{R}_j$: the position of the Tb(j) atom]. Hence, the crystal structure factor is zero, meaning that $\underline{2n+1}00$ reflections are forbidden. However, in the space group *P*4/*mbm* having the twofold screw axis parallel to [100], the anisotropic tensor of susceptibility (ATS) scattering at $\boldsymbol{\tau} = (2n+1, 0, 0)$ is allowed under a resonant condition [18]. The crystal structure factor for the ATS scattering $\hat{F}_{\mathrm{ATS}}$ is given by $[\sum_j e^{2\pi i \boldsymbol{\tau}\cdot\mathbf{R}_j} \hat{T}^j]$. $\hat{T}^j$ is a tensorial scattering factor for Tb(j) site. Each $\hat{T}^j$ is defined by nine components as $T_{\alpha\beta}$ $(\alpha, \beta = x, y, z)$. Here x, y, and z are the local axes of $\hat{T}^j$. When the coordinate axes are set along [110], [1$\bar{1}$0], and [001], the symmetry operations $\mathbf{g}$ for the site symmetry *m*.2*m* of Tb atoms (twofold rotation about [110] and mirror operations normal to [1$\bar{1}$0] and [001]) make off-diagonal components zero by equations $\hat{R}(\mathbf{g})\hat{T}^j\hat{R}^{-1}(\mathbf{g}) = \hat{T}^j$. $\hat{R}(\mathbf{g})$ is the matrix of the symmetry operation $\mathbf{g}$. In addition, four $\hat{T}^j$ are tied by the fourfold symmetry. $\hat{F}_{\mathrm{ATS}}$ at $\boldsymbol{\tau} = (2n+1, 0, 0)$ as a function of the azimuthal angle ψ is expressed as

$$\hat{F}_{\mathrm{ATS}}(0) = \begin{pmatrix} 0 & F_1 & 0 \\ F_1 & 0 & 0 \\ 0 & 0 & 0 \end{pmatrix} \quad \text{and}$$

$$\hat{F}_{\mathrm{ATS}}(\psi) = \begin{pmatrix} 1 & 0 & 0 \\ 0 & \cos\psi & -\sin\psi \\ 0 & \sin\psi & \cos\psi \end{pmatrix} \begin{pmatrix} 0 & F_1 & 0 \\ F_1 & 0 & 0 \\ 0 & 0 & 0 \end{pmatrix} \times \begin{pmatrix} 1 & 0 & 0 \\ 0 & \cos\psi & \sin\psi \\ 0 & -\sin\psi & \cos\psi \end{pmatrix} = \begin{pmatrix} 0 & F_1\cos\psi & -F_1\sin\psi \\ F_1\cos\psi & 0 & 0 \\ -F_1\sin\psi & 0 & 0 \end{pmatrix}, \quad (1)$$

where F_1 is a real number $[F_1 = 2T_{xx}\cos\{2\pi(2n+1)x\}]$. We obtain the scattering matrix $\mathbf{F}$,

$$\mathbf{F} = \begin{pmatrix} F_{\sigma'\sigma} & F_{\sigma'\pi} \\ F_{\pi'\sigma} & F_{\pi'\pi} \end{pmatrix} = \widehat{\boldsymbol{\varepsilon}'} \cdot \hat{F}_{\mathrm{ATS}} \cdot \hat{\boldsymbol{\varepsilon}} = F_1 \sin\psi\cos\theta \begin{pmatrix} 0 & 1 \\ 1 & 0 \end{pmatrix}. \quad (2)$$

Here $\hat{\boldsymbol{\varepsilon}}$ ($\widehat{\boldsymbol{\varepsilon}'}$) denotes the polarization unit vector of the incident (diffracted) x-ray beam, and $F_{\alpha'\beta}$ denotes the scattering amplitude for each polarization state, α' and β. The former is the polarization state of the diffracted x-ray beam and the latter is that of the incident x-ray beam as shown in the inset of Fig. 2.

B. Formulation of the magnetic scattering factor

Using the magnetic structures reported in Ref. [16], we calculate the magnetic structure factor in the AFM1 phase of TbB_4 [see Fig. 1(a)]. In the geometry with the c axis perpendicular to the scattering plane ($\psi = 0$), the magnetic structure factor at $\boldsymbol{\tau} = (2n+1, 0, 0)$ is calculated as

$$\mathbf{F}_m(0) = \sum_j \hat{\mathbf{m}}_j e^{i\boldsymbol{\tau}\cdot\mathbf{R}_j} = \sum_j \mathbf{m}_j \exp 2\pi i(2n+1)x_j = (0,\ iF_{mb},\ 0). \quad (3)$$

Here $\hat{\mathbf{m}}_j$ represents the unit vector along the local magnetic moment of the Tb atom at site j. F_{mb} is a real number. The ψ dependence of $\mathbf{F}_m$ is given by

$$\mathbf{F}_m(\psi) = \begin{pmatrix} 1 & 0 & 0 \\ 0 & \cos\psi & -\sin\psi \\ 0 & \sin\psi & \cos\psi \end{pmatrix} \begin{pmatrix} 0 \\ iF_{mb} \\ 0 \end{pmatrix} = \begin{pmatrix} 0 \\ iF_{mb}\cos\psi \\ iF_{mb}\sin\psi \end{pmatrix}. \quad (4)$$

The sign of $\mathbf{F}_m$ is reversed by time-reversal operation and depends on the time-reversal AFM domain. Following the derivation given in Refs. [21,27–29], we obtain the magnetic scattering matrix $\mathbf{G}$,

$$\mathbf{G} = \begin{pmatrix} G_{\sigma'\sigma} & G_{\sigma'\pi} \\ G_{\pi'\sigma} & G_{\pi'\pi} \end{pmatrix} = \begin{pmatrix} 0 & b\mathbf{F}_m\cdot\hat{\mathbf{q}} \\ -b\mathbf{F}_m\cdot\widehat{\mathbf{q}'} & b\mathbf{F}_m\cdot(\widehat{\mathbf{q}'}\times\hat{\mathbf{q}}) \end{pmatrix} = ibF_{mb}\begin{pmatrix} 0 & \cos\psi\cos\theta \\ -\cos\psi\cos\theta & \sin\psi\sin 2\theta \end{pmatrix}, \quad (5)$$

where b is the dimensionless resonant strength of an electric dipole event, which is expressed as $b = -(3i/4\pi q)(F^1_{-1} - F^1_{+1})$ using the wave number of a photon q and the resonant strengths of the dipole transition F^1_v with a change in magnetic quantum number v.

C. Formulation of the scattering cross section

The total scattering matrix $\mathbf{f}$, which is expressed as the combination of Eqs. (2) and (5), is $\mathbf{f} = \mathbf{F} + e^{i\phi}\mathbf{G}$. Here a phase factor $e^{i\phi}$, which depends on the incident photon energy, is introduced because the ATS and the magnetic scatterings have a different energy dependence to each other. This gives the general cross section with using the Poincaré-Stokes

parameter $\mathbf{P} = (P_1,\ P_2,\ P_3)$ as

$$\begin{aligned}\frac{d\sigma}{d\Omega} &= \frac{1}{2}(1+P_3)(f^*_{\sigma'\sigma}f_{\sigma'\sigma} + f^*_{\pi'\sigma}f_{\pi'\sigma}) \\ &+ \frac{1}{2}(1-P_3)(f^*_{\pi'\pi}f_{\pi'\pi} + f^*_{\sigma'\pi}f_{\sigma'\pi}) \\ &+ P_2\mathrm{Im}[f^*_{\sigma'\pi}f_{\sigma'\sigma} + f^*_{\pi'\pi}f_{\pi'\sigma}] \\ &+ P_1\mathrm{Re}[f^*_{\sigma'\pi}f_{\sigma'\sigma} + f^*_{\pi'\pi}f_{\pi'\sigma}]. \end{aligned} \quad (6)$$

Here $P_1 = \pm 1$ represents the linear polarization of $\pm 45^\circ$ off from the scattering plane, $P_2 = \pm 1$ represents the right- and the left-circular polarization, and $P_3 = \pm 1$ represents the σ and the π linear polarization, respectively.

The π-polarized [$(\mathbf{P} = (0,\ 0,\ -1)$] incident x-rays beam gives the total cross section for $\boldsymbol{\tau} = (2n+1, 0, 0)$, which is the sum of the $\sigma'-\pi$ and $\pi'-\pi$ channels, as

$$\frac{d\sigma}{d\Omega}_{\pi} = f^*_{\pi'\pi}f_{\pi'\pi} + f^*_{\sigma'\pi}f_{\sigma'\pi} = I_{\pi'\pi} + I_{\sigma'\pi}. \quad (7)$$

Here $I_{\pi'\pi}$ and $I_{\sigma'\pi}$ are the intensity of the $\pi'-\pi$ and the the $\sigma'-\pi$ channels, respectively. These intensities are given as

$$I_{\pi'\pi} = F^2_{mb}|b|^2\sin^2 2\theta \sin^2\psi \text{ and} \quad (8)$$

$$\begin{aligned} I_{\sigma'\pi} &= F_1^2\cos^2\theta\sin^2\psi + F^2_{mb}|b|^2\cos^2\theta\cos^2\psi \\ &- 2F_1F_{mb}(\mathrm{Re}[b]\sin\phi + \mathrm{Im}[b]\cos\phi)\sin\psi\cos\psi. \end{aligned} \quad (9)$$

In the paramagnetic phase, the magnetic scattering is absent, i.e., $F_{mb} = 0$, and the intensities are given as

$$I_{\pi'\pi} = 0 \quad \text{and} \quad (10)$$

$$I_{\sigma'\pi} = F_1^2\cos^2\theta\sin^2\psi. \quad (11)$$

In the same way, the circularly polarized incident x-ray beam gives the dichroic intensity for $\boldsymbol{\tau} = (2n+1, 0, 0)$ as

$$\begin{aligned} I_{\mathrm{circ}} &= P_2\mathrm{Im}[f^*_{\sigma'\pi}f_{\sigma'\sigma} + f^*_{\pi'\pi}f_{\pi'\sigma}] \\ &= P_2(-\mathrm{Re}[b]\cos\phi + \mathrm{Im}[b]\sin\phi)F_{mb}F_1\cos\theta \\ &\times \sin 2\theta\ \sin^2\psi. \end{aligned} \quad (12)$$

Thus, the circular-polarization dependent part of the cross section is proportional to a product of the magnetic component F_{mb} and the component in the ATS scattering F_1, meaning that it arises from their interference. In addition, its sign depends on the time-reversal domain where the sign of F_{mb} is revered.

IV. RESULTS AND DISCUSSION

A. Results of Tb L_3 absorption edge

Figure 2(a) shows XAS obtained by x-ray fluorescence spectroscopy. The spectrum exhibits a peak structure centered at the photon energy of incident x rays $E_{\mathrm{ph}} = 7.5175$ keV (E_{L3}), which corresponds to the Tb L_3 absorption edge (vertical broken line in Fig. 2) and is the photon energy we employed for the following measurements. Figure 2(b) displays the photon energy dependence of the integrated intensity of the 200 Bragg reflection measured using π-polarized x rays. The intensity shows a minimum at the energy near the Tb L_3 absorption edge, which is a typical feature of space-group-allowed reflections. Figure 2(c) shows the photon energy profiles of the 300 forbidden reflection obtained with the $\sigma'-\pi$ and the $\pi'-\pi$ channels at 16 K ($< T_{N2}$). The azimuthal angle was set at $\psi \approx -90^\circ$. Unlike the 200 Bragg reflection, the 300 forbidden reflection is enhanced at around the absorption edge for both channels, confirming their origins in the resonance of Tb atoms.

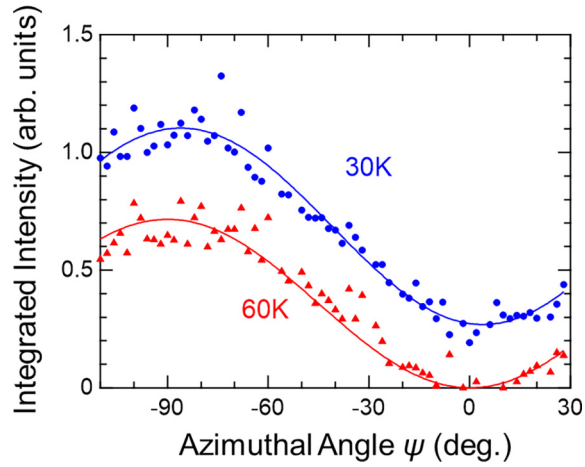

FIG. 3. Azimuthal angle (ψ) dependence of the integrated intensity obtained from the 300 forbidden reflection at 30 K ($< T_{N1}$) and 60 K ($> T_{N1}$). The data were taken for the $\sigma'-\pi$ channel at $E_{\mathrm{ph}} = 7.5175$ keV. The solid curves for 30 and 60 K are fits to the experimental data with Eqs. (9) and (11), respectively.

Figure 3 shows the ψ dependence of the integrated intensity (I) for the 300 forbidden reflection at 30 K ($< T_{N1}$) and 60 K ($> T_{N1}$). The data were taken for the $\sigma'-\pi$ channel at $E_{\mathrm{ph}} = E_{L3}$. At 60 K (paramagnetic phase), the integrated intensity becomes nearly zero at $\psi \approx 0$ and the obtained ψ dependence is well fitted to Eq. (11) (red solid curve in Fig. 3). This means that the 300 reflection is ascribed only to the ATS scattering in the paramagnetic phase. The data at 30 K (AFM1 phase) is shifted significantly in the vertical direction in addition to a slight phase shift. Then the integrated intensity becomes finite at $\psi = 0$. The blue solid curve in Fig. 3 is a fit to the experimental data with Eq. (9). At 30 K, $F^2_{mb}|b|^2/F_1^2 = 0.249$, showing the contribution of both the ATS and the magnetic scatterings in the AFM1 phase. The slight phase shift in the ψ dependence of the integrated intensity is ascribed to the F_1F_{mb} interference term [the last term in Eq. (9)]. This shift depends on the photon energy. It should be noted that the value of F_1^2 at 30 K obtained by the fitting is 1.53 times larger than that at 60 K, which suggests that the ATS scattering is enhanced below T_{N1}. In fact, Ref. [19] reports on the enhancement of the ATS signal at the Tb M_5 edge below T_{N1}. These results show that the 300 reflection is ascribed only to the ATS scattering in the paramagnetic phase and both the ATS and the magnetic scatterings in the AFM1 phase.

Figure 4 shows the temperature evolution of the 300 forbidden reflection obtained at $E_{\mathrm{ph}} = E_{L3}$ and $\psi = -90^\circ$ with three different polarization settings. Figures 4(a) and 4(b) display the peak profiles at several temperatures and the temperature dependence of the integrated intensity, respectively, taken in

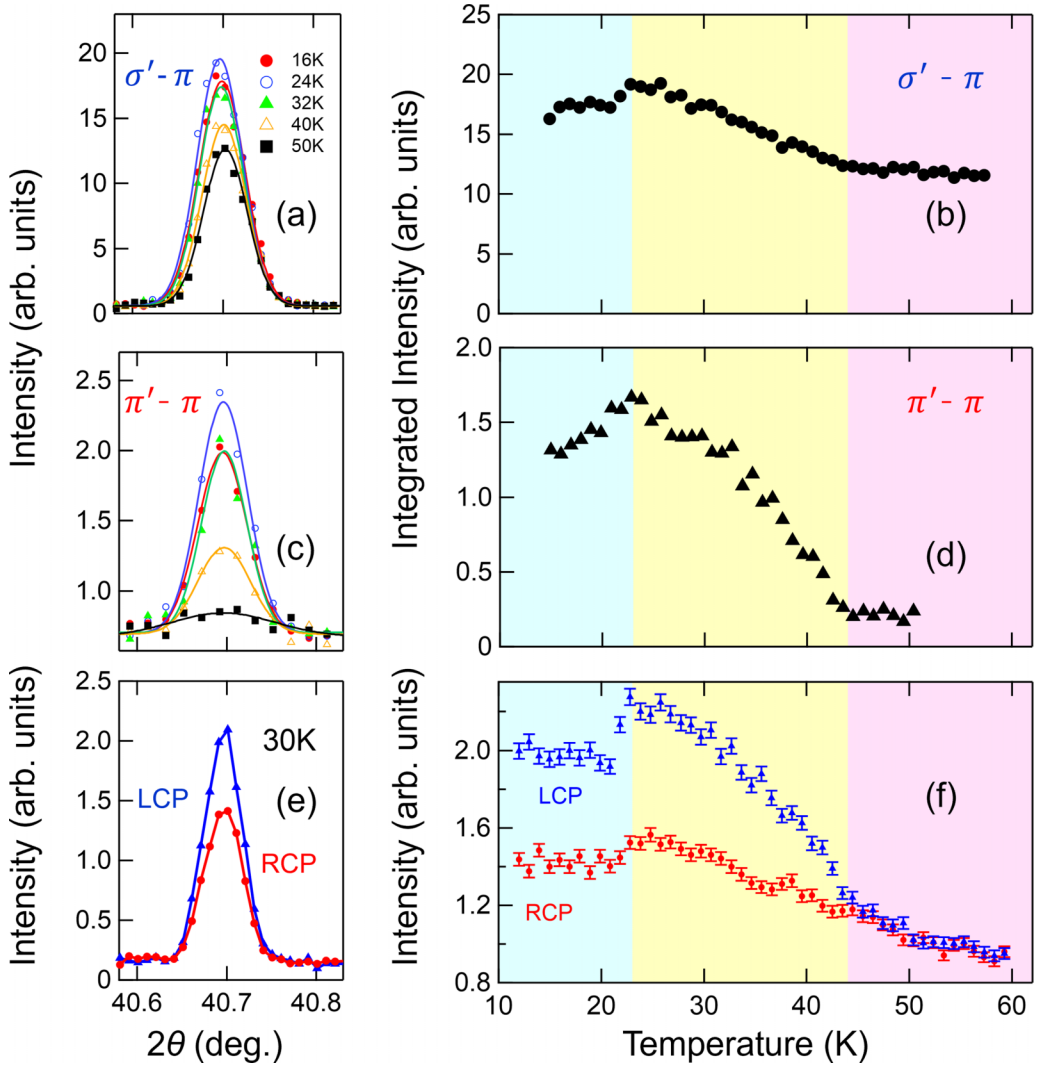

FIG. 4. (a)–(d) Temperature evolution of the 300 forbidden reflection obtained for the $\sigma'-\pi$ (blue) and the $\pi'-\pi$ channels at $\psi = -90°$. The data were taken at $E_{ph} = 7.5175$ keV during warming. (a), (c) Peak profiles of the 300 reflection at selected temperatures for the $\sigma'-\pi$ (a) and the $\pi'-\pi$ (c) channels. Solid curves are fits to Gaussian functions. (b), (d) Integrated intensity of the 300 reflection as a function of temperature for the $\sigma'-\pi$ (b) and the $\pi'-\pi$ (d) channels. (e), (f) Temperature evolution of the 300 forbidden reflection obtained at $\psi = -90°$ using LCP and RCP incident x rays. (e) Peak profiles at 30 K ($< T_{N1}$). (f) Integrated intensity of the 300 reflection as a function of temperature.

the $\sigma'-\pi$ channel. Equation (9) gives $I_{\sigma'\pi} = F_1^2\cos^2\theta$ at $\psi = -90°$, where only the ATS scattering contributes to the 300 reflection in the $\sigma'-\pi$ channel. Thus, Fig. 4(b) shows that the contribution of the ATS scattering is finite and weakly temperature dependent at temperatures above T_{N1} and is remarkably enhanced below T_{N1}. Such an enhancement of F_1^2 in the AFM1 phase is quantitively consistent with the result obtained from the fitting to the ψ dependence of the integrated intensity shown in Fig. 3 (see the previous paragraph). With further lowering temperature, the integrated intensity is slightly decreased below T_{N2}, which implies a suppression of the ATS scattering in the AFM2 phase. Figures 4(c) and 4(d) display the results taken in the $\pi'-\pi$ channel. Equation (8) gives $I_{\pi'\pi} = F_{mb}^2|b|^2\sin^2 2\theta$ at $\psi = -90°$, where only the magnetic scattering contributes to the 300 reflection in the $\pi'-\pi$ channel. Thus, Fig. 4(d) shows that almost no magnetic scattering signal was observed at temperatures above T_{N1}, but the intensity develops below T_{N1}. Note that a weak peak is seen in the data at 50 K ($> T_{N1}$) [Fig. 4(c)] and the integrated intensity at temperatures above T_{N1} is finite [Fig. 4(d)], which originates from the ATS scattering due to the leakage contribution of the $\sigma'-\pi$ channel. As is the case for the $\sigma'-\pi$ channel, the integrated intensity for the $\pi'-\pi$ channel is suppressed below T_{N2}, suggesting a correlation between the ATS and the magnetic scatterings.

Next, we carried out measurements using circularly polarized incident x rays to confirm that the interference effect between the ATS and the magnetic scatterings leads to the circular polarization dependence on the 300 reflection as expected from Eq. (12). The azimuthal angle was fixed at $\psi = -90°$ where the interference effect is anticipated to be the maximum. The energy of incident x rays was tuned to E_{L3}. The degree of circular polarization for the incident x rays was $|P_2| \gtrsim 0.98$. To exclude the effect of mixed domain states, the

incident beam was narrowed down to 20 μm × 20 μm in area by using a pinhole. Figure 4(e) shows the peak profile of the 300 reflection obtained at 30 K with LCP and RCP incident x rays. A clear circular polarization dependence with larger intensity for LCP x rays is evident. Figure 4(f) shows the temperature dependence of the 300 reflection intensities for LCP and RCP incident x rays. While there is no difference in the data obtained with RCP and LCP x rays above T_{N1}, the relative difference develops below T_{N1} and reaches about 20% at around T_{N2}. Note that the sign of the circular dichroism depends on the sample position, which was confirmed by the measurements at different sample positions (not shown). According to Eq. (12), the sign of the circular dichroism depends on that of $\mathbf{F}_m$, which means that the observed circular dichroic signals reflect the AFM domain state. Thus, in principle, scanning x-ray microdiffraction measurements using circularly polarized incident x rays enable us to clarify spatial distributions of time-reversal AFM domains in TbB_4. However, the present experimental setup for the measurements in the vicinity of the Tb L_3 absorption edge was not suitable for microscopy because of the weak intensity of the narrowed incident beam and the sample drifting.

B. Results of Tb M_5 absorption edge

To further clarify the effect of AFM domains on circular dichroism and to spatially resolve the domain structure, we conducted experiments using soft x rays whose energy was tuned in the vicinity of the Tb $M_{4,5}$ edges. The instrument used in this experiment is more suitable for scanning resonant x-ray microdiffraction measurements because the incident beam can be focused to a size of 25 μm × 10 μm in area by the upstream Kirkpatrick-Baez mirrors [25,30]. First, we clarify the energy and the temperature profiles of the 100 reflection using an unfocused x-ray beam. Figure 5(a) shows XAS in which prominent peaks appear around Tb M_5 and M_4 edges. Figure 5(b) shows the energy profile of the intensity of the 100 forbidden reflection at three different temperatures. At 50 K (paramagnetic phase), the reflection intensity shows a maximum centered at $E_{ph} \approx 1237.5$ eV, which is ascribed to the ATS scattering. On the other hand, it shows a peak at $E_{ph} \approx 1240.0$ eV in the AFM phases (30 and 20 K), which mainly originates from the magnetic scattering. The intensity in the paramagnetic phase is two orders of magnitude smaller than that in the AFM phases. This suggests that the magnetic contribution is much larger than the ATS contribution at the Tb M_5 edge. The enhancement of the 100 reflection in the AFM phases is clearly seen in Fig. 5(c) which shows the temperature dependence of the integrated intensity of the 100 reflection at $E_{ph} = 1237.5$ eV. Unfocused RCP incident x rays were used for this measurement. Figure 5(d) displays rocking curves obtained in the three different phases. The reflection intensity starts to develop below T_{N1}, shows a kink at T_{N2}, and further increases with cooing down to the lowest temperature.

Finally, we visualize spatial distributions of the time-reversal AFM domains using circular dichroic signals ascribed to the interference between the ATS and the magnetic scatterings. To spatially resolve the distribution of AFM domains, we carried out scanning microdiffraction measurements on the (100) face of a specimen with a focused x-ray

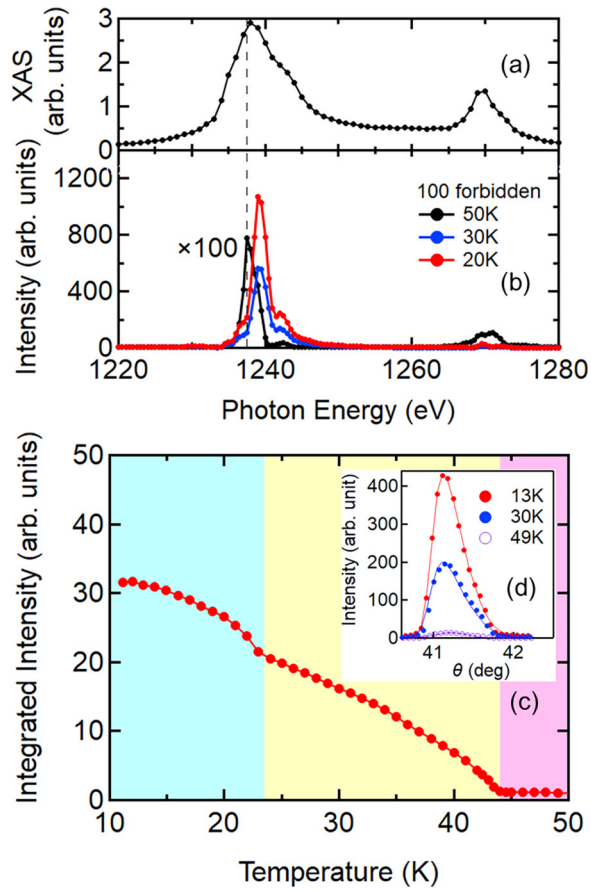

FIG. 5. (a), (b) Photon energy profiles near the Tb $M_{4,5}$ edges in TbB_4. (a) X-ray absorption spectrum (XAS) obtained by measuring the fluorescence yield at room temperature. (b) Integrated intensity of the 100 forbidden reflection. Spectrum at 50 K is multiplied by 100 for ease of eyes. The vertical broken line in (a) and (b) denote the photon energy used for the measurement of panels (c) and (d). (c), (d) Temperature evolution of the 100 forbidden reflection obtained using LCP incident x rays with $E_{ph} = 1237.5$ eV. (c) Integrated intensity of the 100 reflection as a function of temperature. (d) Rocking curves of the 100 reflection at 13, 30, and 49 K.

beam at 30 K. The photon energy of x rays was set at 1237.5 eV where the ATS scattering on the 100 reflection is the most enhanced [see Fig. 5(b)] and the interference between the ATS and the magnetic scatterings is significant. The maps shown in Figs. 6(a) and 6(b) were taken at the same sample area by using RCP and LCP incident x rays, respectively. Bright and dark regions in the maps correspond to high- and low-intensity counts, respectively, whose contrast is expected from the interference between the ATS scattering and the magnetic scattering. The black and white contrast is reversed from Fig. 6(a) to Fig. 6(b), which confirms that the maps correspond to spatial distributions of the time-reversal AFM domains. Figures 6(c) and 6(d) are the line profiles along the Z direction ($\parallel b$) and the Y direction ($\parallel c$), respectively. These line profiles suggest that the domain size along the Z direction ($\parallel b$) is larger than that along the Y direction ($\parallel c$), which is also evident in the two-dimensional maps shown in Figs. 6(a) and 6(b). From these results, time-reversal AFM domains in TbB_4 are platelike in shape: the plates are parallel

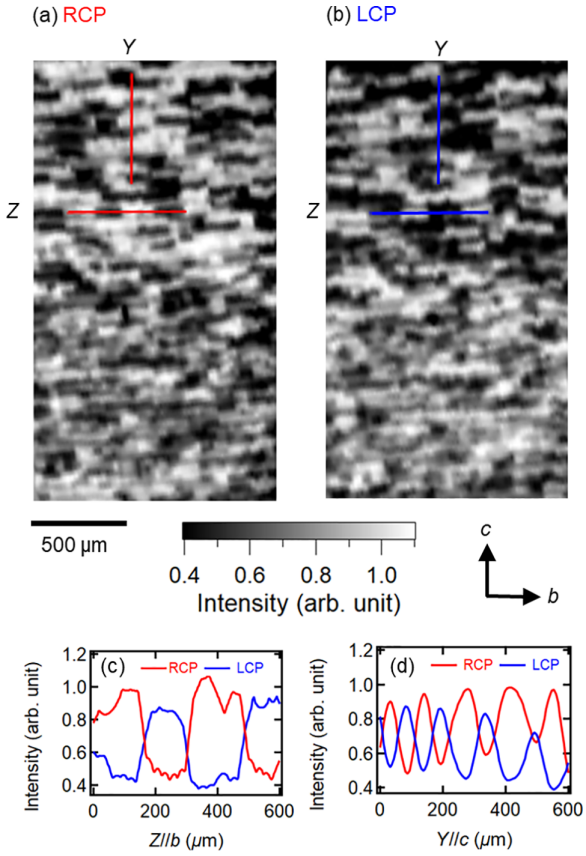

FIG. 6. Time-reversal antiferromagnetic domains in the AFM1 phase of TbB_4. (a), (b) Two-dimensional maps of the intensity of the 100 forbidden reflection. These measurements were performed at 30 K using (a) RCP and (b) LCP x rays with $E_{ph} = 1237.5$ eV. (c), (d) Line profiles of the intensity obtained with RCP and LCP incident x rays at red lines Z (//b) and Y (//c) in panels (a) and (b).

to the ab plane and are stacking along the c axis. Very recently, AFM domain structures on the ab face of a TbB_4 crystal have been revealed by the observation of nonreciprocal rotation of reflected light (NRR) [31], which shows that irregular-shape domains with the size ranging from several tens to hundreds of micrometers are distributed on the ab face without clamping along specific crystallographic axes. The domain size along the b axis in the present study is essentially consistent with the result of the NRR measurement. The platelike domain structure is probably attributed to anisotropic nature of magnetic interactions in TbB_4.

V. CONCLUSIONS

We investigated resonant x-ray diffraction (RXD) on a single crystal of TbB_4 showing antiferromagnetic (AFM) orders breaking both time-reversal and space-inversion symmetries. We show the contributions of the ATS and the magnetic scatterings to *odd*00 reflections in both the Tb L_3 and the M_5 edges. Through the interference between the ATS and the magnetic scattering, the circular polarization dependence of RXD was observed at *odd*00 reflections. The results demonstrate that the circularly polarized RXD technique enables us to detect not only the magnitude but also the sign of the AFM order parameter of TbB_4. Adopting this technique to scanning microdiffraction measurements, we succeeded in visualizing spatial distributions of the time-reversal (or space-inversion) AFM domains on the (100) face of a TbB_4 crystal. The observed domains appeared to be plate shaped and to stack along the c axis, which may reflect the anisotropic nature of magnetic interactions of the rare-earth tetraboride. The present study reveals that circularly polarized RXD using the interference effect between the ATS and the magnetic scatterings is a powerful tool to detect AFM order parameters and spatially resolve AFM domain structures in materials without space-inversion and time-reversal symmetries, giving rise to a variety of functionalities.

ACKNOWLEDGMENT

We thank M. Oura and Y. Kohmura for their help in the experiments and M. Suzuki for helpful discussions. The images of crystal structures were drawn using the software VESTA [32]. This work was supported by JSPS KAKENHI Grants No. JP19H00661, No. JP19H05823, and No. JP21H04436. Hard and soft x-ray experiments were performed at the beamlines 19LXU 17SU in SPring-8, respectively, with the approval from RIKEN (Proposals No. 20210009 and No. 20220014).

[1] J. Etourneau and P. Hagenmuller, Philos. Mag. B **52**, 589 (1985).
[2] S. Gabani, K. Flachbart, K. Siemensmeyer, and T. Mori, J. Alloy Compd. **821**, 153201 (2020).
[3] *Rare-Earth Borides*, edited by D. S. Inosov (Jenny Stanford, Singapore, 2021).
[4] Z. Fisk, M. B. Maple, D. C. Johnston, and L. D. Woolf, Solid State Commun. **39**, 1189 (1981).
[5] S. Yoshii, T. Yamamoto, M. Hagiwara, S. Michimura, A. Shigekawa, F. Iga, T. Takabatake, and K. Kindo, Phys. Rev. Lett. **101**, 087202 (2008).
[6] K. Siemensmeyer, E. Wulf, H.-J. Mikeska, K. Flachbart, S. Gabáni, S. Mat'aš, P. Priputen, A. Efdokimova, and N. Shitsevalova, Phys. Rev. Lett. **101**, 177201 (2008).
[7] S. Yoshii, K. Ohoyama, K. Kurosawa, H. Nojiri, M. Matsuda, P. Frings, F. Duc, B. Vignolle, G. L. J. A. Rikken, L.-P. Regnault, S. Michimura, and F. Iga, Phys. Rev. Lett. **103**, 077203 (2009).
[8] H. Sim, S. Lee, K.-P. Hong, J. Jeong, J. R. Zhang, T. Kamiyama, D. T. Adroja, C. A. Murray, S. P. Thompson, F. Iga, S. Ji, D. Khomskii, and J.-G. Park, Phys. Rev. B **94**, 195128 (2016).
[9] S. Ji, C. Song, J. Koo, K.-B. Lee, Y. J. Park, J. Y. Kim, J.-H. Park, H. J. Shin, J. S. Rhyee, B. H. Oh, and B. K. Cho, Phys. Rev. Lett. **91**, 257205 (2003).
[10] D. Okuyama, T. Matsumura, H. Nakao, and Y. Murakami, J. Phys. Soc. Jpn. **75**, 198 (2006).
[11] S. Ji, C. Song, J. Koo, J. Park, Y. J. Park, K.-B. Lee, Seongsu Lee, J.-G. Park, J. Y. Kim, B. K. Cho, K.-P. Hong, C.-H. Lee, and F. Iga, Phys. Rev. Lett. **99**, 076401 (2007).

[12] S. W. Lovesey, J. Fernández Rodriguez, J. A. Blanco, and P. J. Brown, Phys. Rev. B **70**, 172414 (2004).
[13] S. W. Lovesey, E. Balcar, K. S. Knight, and J. Fernández, Phys. Rep. **411**, 233 (2005).
[14] J. A. Blanco, P. J. Brown, A. Stunault, K. Katsumata, F. Iga, and S. Michimura, Phys. Rev. B **73**, 212411 (2006).
[15] H. Watanabe and Y. Yanase, Phys. Rev. B **98**, 245129 (2018).
[16] T. Matsumura, D. Okuyama, and Y. Murakami, J. Phys. Soc. Jpn. **76**, 015001 (2007).
[17] T. Suzuki, T. Fujira, I. Ishii, S. Michimura, F. Iga, and T. Takabatake, J. Phys.: Conf. Ser. **150**, 042194 (2009).
[18] V. E. Dmitrienko, Acta Cryst. A **39**, 29 (1983).
[19] H. Huang, H. Jang, B. Y. Kang, B. K. Cho, C.-C. Kao, Y.-J. Liu, and J.-S. Lee, Curr. Appl. Phys. **18**, 1205 (2018).
[20] S. Tardif, S. Takeshita, H. Ohsumi, J.-I. Yamaura, D. Okuyama, Z. Hiroi, M. Takata, and T.-H. Arima, Phys. Rev. Lett. **114**, 147205 (2015).
[21] H. Ueda, Y. Tanaka, Y. Wakabayashi, and T. Kimura, Phys. Rev. B **98**, 134415 (2018).
[22] F. Iga, N. Shimizu, and T. Takabatake, J. Magn. Magn. Mater. **177**, 337 (1998).
[23] T. K. Fujita, M. Yoshizawa, R. Kamiya, H. Mitamura, T. Sakakibara, K. Kindo, F. Iga, I. Ishii, and T. Suzuki, J. Phys. Soc. Jpn. **80**, SA084 (2011).
[24] K. Hirano, Jpn. J. Appl. Phys. **36**, L637 (1997).
[25] T. Takeuchi, A. Chainani, Y. Takata, Y. Tanaka, M. Oura, M. Tsubota, Y. Senba, H. Ohashi, T. Mochiku, K. Hirata, and S. Shin, Rev. Sci. Instrum. **80**, 023905 (2009).
[26] K. Shirasawa, T. Tanaka, T. Seike, A. Hiraya, and H. Kitamura, AIP Conf. Proc. **705**, 203 (2004).
[27] S. W. Lovesey and S. P. Collins, *X-ray Scattering and Absorption by Magnetic Materials* (Oxford Science, Clarendon Press, Oxford, 1996).
[28] H. Nakajima, T. Usui, Y. Joly, M. Suzuki, Y. Wakabayashi, T. Kimura, and Y. Tanaka, Phys. Rev. B **93**, 144116 (2016).
[29] R. Misawa, H. Ueda, K. Kimura, Y. Tanaka, and T. Kimura, Phys. Rev. B **103**, 174409 (2021).
[30] Y. Hiraoka, Y. Tanaka, T. Kojima, Y. Takata, M. Oura, Y. Senba, H. Ohashi, Y. Wakabayashi, S. Shin, and T. Kimura, Phys. Rev. B **84**, 064418 (2011).
[31] K. Arakawa, T. Hayashida, K. Kimura, R. Misawa, T. Nagai, T. Miyamoto, H. Okamoto, F. Iga, and T. Kimura (unpublished).
[32] K. Momma and F. Izumi, J. Appl. Cryst. **44**, 1272 (2011).